An Open Model of Actin Dendritic Nucleation

Jonathon A. Ditlev, Nathaniel M. Vacanti, Igor L. Novak, and Leslie M. Loew*
Richard D. Berlin Center for Cell Analysis and Modeling, University of Connecticut Health Center, Farmington, CT 06030-1507

ABSTRACT The availability of quantitative experimental data on the kinetics of actin assembly has enabled the construction of many mathematical models focused on explaining specific behaviors of this complex system. However these ad hoc models are generally not reusable or accessible by the large community of actin biologists. In this work, we present a comprehensive model that integrates and unifies much of the in vitro data on the components of the dendritic nucleation mechanism for actin dynamics. More than 300 simulations have been run based on compartmental and three-dimensional spatial versions of this model. Several key findings are highlighted, including an explanation for the sharp boundary between actin assembly and disassembly in the lamellipodia of migrating cells. Because this model, with the simulation results, is "open source", in the sense that it is publicly available and editable through the Virtual Cell database (http://vcell.org), it can be accessed, analyzed, modified, and extended.

INTRODUCTION

External signals at the leading edge of a migrating cell activate the Arp2/3 complex at the cytoplasmic face of the plasma membrane, which then binds to actin filaments and nucleates new F-actin (1,2). This produces a dense, highly branched actin polymer network in the lamellipodium (2–5). Rapid accumulation of F-actin at the leading edge results in rearward movement of this network and can provide a protrusive force that drives the lamellipodium forward (4,6–8). Morphologically, the lamellipodium is revealed by electron microscopy as a thin, dense meshwork of filaments composed of relatively short segments compared to less branched, longer F-actin distributions to the rear of the cell (9).

Modeling and simulation of actin dynamics (7) benefits from a wealth of quantitative in vitro data on the kinetics of polymerization in the presence of actin-binding proteins (3–5). These models range from detailed discrete models that follow individual filaments (10–12) to continuum models that can recapitulate in vitro experiments on steady-state distributions of filament size and turnover (13–15). Constructing a model that can approximate the in vivo behavior is daunting, however, because of the large number of interacting components. One common strategy for modeling the cellular behavior is to avoid the details and develop phenomenological mathematical models that use physical principles to reproduce a specific cellular mechanism. This approach has indeed proven powerful in suggesting or explaining experiments. For example, recent studies have shown how models with a relatively small number of variables that abstract essential features of actin dynamics can explain the variable shape of motile keratocytes (16), show that G-actin diffusion is sufficient to deliver monomers to the actively polymerizing leading edge (17), explain the relationship of protrusion velocity and the concentration of barbed ends (14), or explain the relationship between severing and capping in controlling acting polymerization (18).

But such lumped models cannot probe for how the detailed interactions of multiple molecular components affect the behavior of the entire system. Therefore, they cannot always be used to directly interpret the results of experiments on cell physiology that have been made possible via the use of fluorescent probes and quantitative microscopy. Indeed, it has been argued (19) that to fully describe a physiological system (and to design interventions for any pathophysiology), a full inventory of the participating molecules, their structures, and their reactions would be required, culminating in a mathematical model that reproduces the experimentally observable physiology. We would add to this by pointing out that if the model fails to reproduce the physiology, the system components are either incorrect or incomplete; the way that it fails should guide the design of new experiments to correct the mistakes or expose the missing pieces. Furthermore, numerical experiments such as virtual knockouts or altering rate constants in model simulations can reveal the origin of emergent properties of the system. Finally, a comprehensive mathematical model also can serve to collect and organize experimental data on the individual molecular mechanisms comprising a complex physiological process, thus serving as an accessible framework for data derived from diverse sources.

In this work, we present a detailed quantitative model that integrates and unifies much of the in vitro data on the components of the dendritic nucleation mechanism for actin dynamics. The model explicitly incorporates the following mechanisms (displayed as a network diagram in Fig. 1): activation of Arp2/3 at the cell membrane by a nucleation promoting factor (e.g., N-WASP) (20–22); nucleation and branching on preexisting F-actin by activated Arp2/3 and two actin monomers (including profilin-bound G-actin) (21,23); dissociation of Arp2/3 branches in the cytoplasm

Submitted September 19, 2008, and accepted for publication January 23, 2009.

*Correspondence: les@volt.uchc.edu

Editor: Alexander Mogilner.

0006-3495/09/05/3529/14 $2.00

doi: 10.1016/j.bpj.2009.01.037

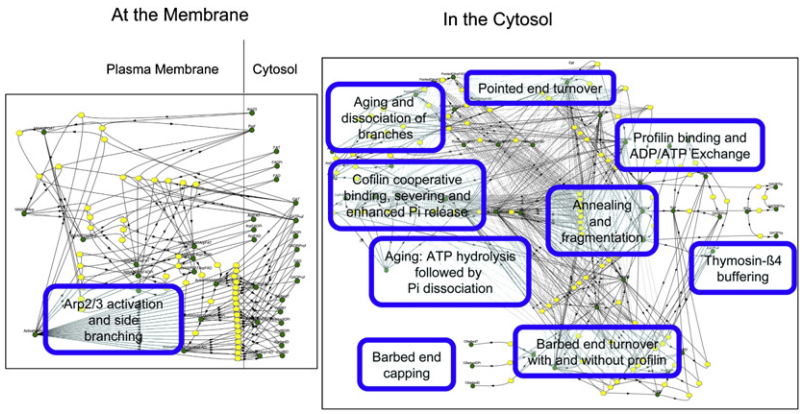

FIGURE 1 Reaction diagram for the dendritic actin nucleation pathway taken from the Virtual Cell model. Each green circle represents a distinct species or state variable. Each yellow oval represents a transformation or reaction. The solid lines connecting the species to the reactions represent the stoichiometry of each reaction. The dashed lines are directed from species that modulate a reaction without actually being consumed or produced. The reactions labeled ''At the Membrane'' depict species that are confined to the membrane surface but can interact with several species in the cytosol, as shown. The blue-framed boxes are labels corresponding to the particular mechanisms of the dendritic nucleation model in that general region of the diagram. Each of these is associated with the corresponding literature citations in Table S2. The expressions and rate constants for each reaction are also provided in Table S2. The rate expressions underlying each reaction are also accessible by double clicking their respective yellow icons in the public Biomodel called ''Actin Dendritic Nucleation_Detailed Branching'' under username ''les'' in the Virtual Cell database (http://vcell.org).

(24); interconversions between the ATP, ADP, and ADP Pi forms of both monomeric G-actin and filamentous F-actin (25–28); assembly and disassembly of these three nucleotide-bound monomer forms to each of the three forms of barbed and pointed ends (i.e., 18 unique pairs of forward and reverse reactions) (29,30); acceleration of nucleotide exchange on G-actin by profilin (25,31,32); addition of G-actin associated with profilin to barbed ends (30,31,33); capping of the three forms of barbed ends (34–36); length-dependent annealing and fragmentation of actin filaments (37,38); buffering of G-actin by thymosin-β4 (33,39,40); severing and accelerated disassembly of actin filaments by actin-depolymerizing factor (ADF)/cofilin (18,32,41–47). The model is implemented in the Virtual Cell modeling and simulation software (48–50). Additionally, we applied this biochemistry to a series of compartmental and three-dimensional (3D) spatial instantiations of the model to produce over 500 simulations that are also stored in the Virtual Cell database. We will highlight several of these simulations to illustrate how the model can recapitulate and help explain in vivo measurements of lamelipodial actin dynamics. Because this model will be ''open source'', in the sense that it will be publicly available and editable through the Virtual Cell database (http://vcell.org), we anticipate that it will be reused and enhanced by many other investigators.

METHODS

The Virtual Cell modeling and simulation software was used for this work (http://vcell.org). The individual biochemical mechanisms and their kinetic constants were based on published data, as detailed in the ''Table of Mechanisms'' provided in the Supporting Material. This table provides the stoichiometry, rate expressions, parameter values, and literature references for each of the reactions in the model, grouped according to the mechanism in Fig. 1. A separate table in the Supporting Material provides definitions of all the species, variable, and function names. To establish the steady-state distributions of species before activation of Arp2/3 with N-WASP, we solved the system of ordinary differential equations (ODE) of the reaction network with many combinations of concentrations for the key molecules using the CVODE solver available in Virtual Cell. These results are collected in an application called ''Steady State Turnover'' within a BioModel entitled *Actin Dendritic Nucleation_Detailed Mechanism* that is accessible in the Virtual Cell database. A second BioModel was developed with an alternative reduced mechanism of Arp2/3 activation and branching, as discussed in the text and which was used to generate Fig. S2 in the Supporting Material. This BioModel, entitled *Actin Dendritic Nucleation*, is also publically available in the Virtual Cell database. A number of ODE simulations are available in a series of Applications entitled ''NWasp Activation…'' for a variety of capping protein (Cap), profilin, Arp2/3, and ActiveNWASP concentrations; a subset of these formed the basis of Fig. 3. A spatial application called ''NWASP at Lam Tip in 3D Geometry'' is also to be found under this BioModel; it associates the biochemistry with the 3D geometry shown in Fig. 4 and also applies the band of ActiveNWASP to the tip of the lamellipodium. This model was not simulated, but was used to generate the initial math description for a public MathModel called ''Actin Advection and Diffusion'', which was then modified to incorporate advection terms and the expression for diffusion of the F-actin species. Simulations of the resultant system of partial differential and algebraic equations was solved with the finite volume solver available in Virtual Cell (48,49, 51–53), using a regular rectangular grid of 90,000 elements and 0.02 s time steps. The simulations were checked with finer mesh and shorter time steps, and the resultant simulations differed from the standard settings by never more than 3%. After activation of Arp2/3 by N-WASP, simulations were run for 3900 s to achieve a steady state within the 3D volume. To see the relaxation behavior of this system, an additional 100 s followed during which the activation of Arp2/3 by N-WASP was stopped (for a total of 4000 s of simulation time). The computations were carried out on the CCAM compute cluster; a single computation required 20 days of compute time, but 20 simulations were typically run in parallel. Additionally, the model in which the periphery is uniformly activated can be formulated as a two-dimensional (2D) model by taking advantage of the cylindrical symmetry of this system, as described in the Supporting Material; this 2D model requires just 6 h of compute time and is available in the Virtual Cell database as a MathModel entitled ''Actin Advection and Diffusion 2D Cylindrical Transform''. The models are available in the Virtual Cell database (http://vcell.org) under username ''les''.

RESULTS

Modeling actin biochemistry

We intended the model to address questions at a whole-cell level, where the number of molecules makes a discrete

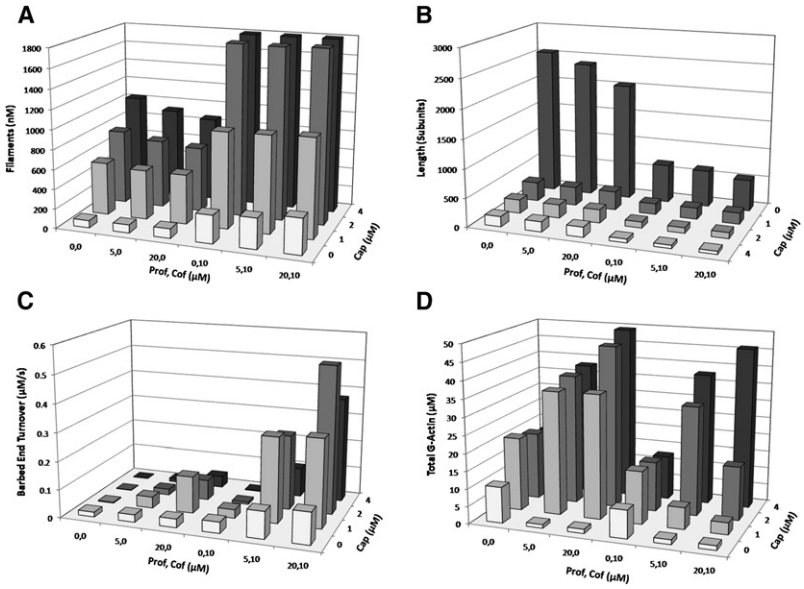

FIGURE 2 Steady-state values for filament concentration, filament length, end turnover, and total monomeric actin as a function of Cap, cofilin, and profilin. The rate for activation of Arp2/3 by N-WASP was set to 0 for these simulations. Total actin was set to 200 μM and thymosin-β4 were set at 200 μM and 100 μM, respectively, at the beginning of each simulation and allowed to equilibrate for 10,000 s at which time all the species had attained steady-state levels. Free ATP, ADP, and Pi were clamped at 10 mM, 2 mM, and 2 mM, respectively. (*A*) Filament concentration is calculated by taking the sum of the concentrations of the three nucleotide forms of pointed ends (equal to the sum of nucleotide forms of capped and uncapped barbed ends). (*B*) The filament length is calculated from the state variables by taking the sum of all forms of F-actin and dividing it by the filament concentration. (*C*) The barbed end turnover was calculated from the sum of 36 individual rates (18 reactions) for the addition (given a positive value) and dissociation (assigned a negative value) of the three forms of G-actin and the three forms of profilin-G-actin to the three forms of barbed ends; these positive rates were exactly balanced by the negative rates associated with the corresponding addition and dissociation of G-actin at pointed ends. (*D*) The total G-actin is the sum of all nucleotide forms including free and bound to profilin and thymosin-β4.

treatment intractable. Therefore, we formulated the system as a continuum model consisting of systems of differential equations. This necessitated the formulation of approaches that could consolidate the infinite number of possible states of actin to a reduced set of variables. We therefore did not attempt to keep track of the individual lengths and positional nucleotides composition of actin filaments. Rather we expressed the concentrations of actin in the different nucleotide forms as lumped variables in terms of the concentration of actin subunits. For example, the state variables FAT, FAD, and FADPi are the total concentration of actin subunits in the filamentous form bound to, respectively, ATP, ADP, and ADPPi (in general, the suffix T, D, or DPi, respectively, denotes the nucleotide form of the various molecular species in the model). The hydrolysis of ATP to ADPPi and the dissociation of the ADPPi forms to ADP are explicitly included in the reaction network for all the actin species. We independently kept track of the concentration of barbed and pointed ends in each of the nucleotide-bound forms; these depend on both the hydrolysis and dissociation reactions of the nucleotide as well as the addition or dissociation of the various nucleotide forms of monomers. Thus, there are 18 separate reactions in the network for addition-dissociation of barbed ends, corresponding to the three nucleotide forms of the ends reacting with the three nucleotide forms for G-actin and the three nucleotide forms of the G-actin-profilin complex. The yellow ovals corresponding to each of these reactions are arrayed near the blue mechanism label ''Barbed end turnover with and without profilin'' in Fig. 1; this label also overlays the yellow reaction ovals corresponding to the

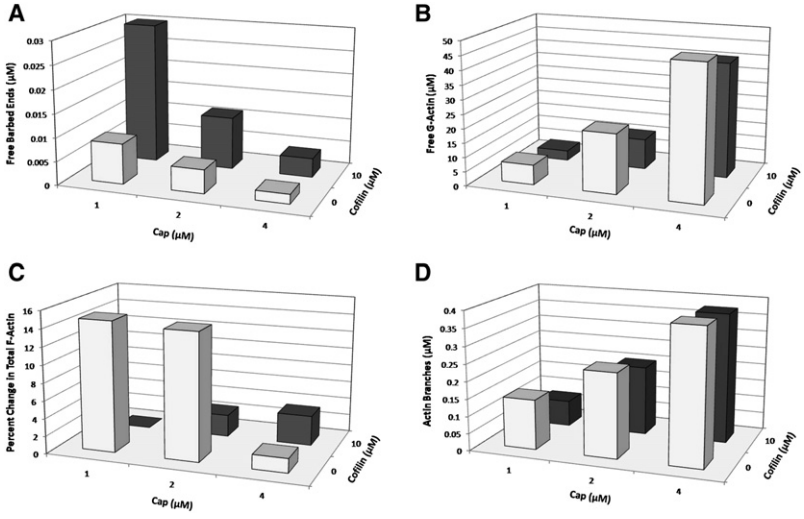

FIGURE 3 The effects of Cap and cofilin on actin polymerization after Arp2/3 activation. All these simulations were carried out with concentrations of total Arp2/3 (inactive + active + incorporated in branches) of 1 μM; ActiveNWASP of 1000 molecules/μm^2; total actin, 200 μM; thymosin-β4, 100 μM; profilin, 20 μM. (*A*) Free-barbed ends. (*B*) G-actin. (*C*) Change in total F-actin relative to the steady state before activation. (*D*) Concentration of branches.

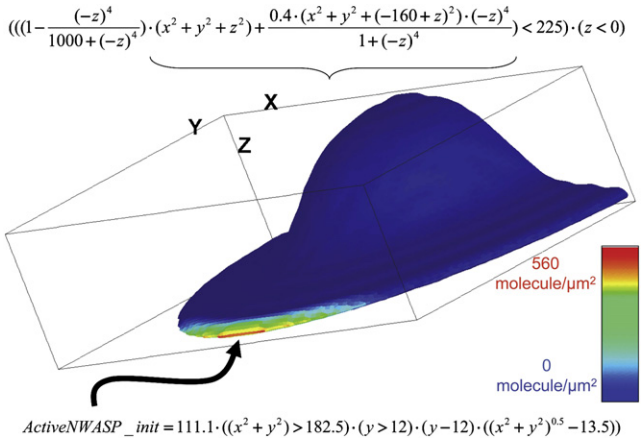

FIGURE 4 The cell-like spatial geometry for the reaction-diffusion-advection model. The geometry is adapted from a public Virtual Cell 3D geometry originally formulated by Jason Haugh (see Biomodel "PDGF Gradient Sensing" under username "jmhaugh"). The expression defining the geometry is shown at the top (units of x,y,z is μm) and the image depicts a surface rendering; the cytosolic compartment is defined at all points where the expression evaluates to TRUE (assigned a numerical value of 1), and the plasma membrane is the surface where the expression transitions from true to false (i.e., a value of 0). Polymerization is triggered at the leading edge by ActiveNWASP (molecules/μm^2) as depicted by the color scale and as defined by the expression at the bottom of the figure. This corresponds to 7246 molecules of ActiveNWASP molecules in a graded distribution within a 46 μm^2 band of membrane.

phosphate hydrolysis and dissociation of the nucleotide on the barbed end species.

The total concentration of subunits in actin filaments is given by the sum of all the state variables corresponding to different forms of F-actin, including all forms of free and capped ends, Arp2/3-bound and cofilin-bound subunits. The concentration of filaments can be calculated from the sum of all the pointed ends, i.e., in all three nucleotide forms and both free and Arp2/3-capped in branches. The average filament length, in number of subunits, is given by the total concentration of F-actin divided by the concentration of filaments. The variable and function names were chosen to be reasonably self-explanatory, but a complete set of definitions is provided in Table S1 in the Supporting Material. Using this approach, we could derive expressions for all the kinetic laws associated with the mechanisms in Fig. 1. This figure is provided as an indication of the complexity of the model and as a guide to the interactive reaction editor screen in Virtual Cell (from which it was derived). All these rate expressions along with the relevant literature references are provided in Table S2 in the Supporting Material and are also available in the Virtual Cell BioModel "Actin Dendritic Nucleation_Detailed Branching" by double clicking the yellow icons in the reaction editor screen. Because most of these mechanisms have been studied with various techniques and with proteins derived from a variety of organisms, we had to choose a subset of these for the model; priority was given to studies where the rates and concentration were explicitly incorporated into a kinetic scheme and, when possible, where the measurements were made on proteins derived from vertebrate nonmuscle cells. Brief narrative descriptions of each mechanism and assumptions that were used to implement them in our model are also included in the Supporting Material.

As described above, we explicitly modeled the association and dissociation of individual nucletotide forms of subunits to individual nucleotide forms of the barbed and pointed ends. A particular difficulty within the model concerned how to express the stoichiometry of the dissociation of actin subunits from the filament ends. Whereas the model explicitly accounts for the individual nucleotide states of all the barbed and pointed ends because the rates of dissociation are dependent on the bound nucleotide, the rest of the F-actin nucleotide state distribution was lumped into just the three state variables, FAT, FAD, and FADPi. For example, the dissociation of BarbedT (i.e., a barbed end in the ATP form) will produce one molecule of GAT (G-actin bound to ATP) plus a new barbed end that can be in any of the three nucleotide states. To precisely define the stoichiometry of this reaction, we would need to track the concentrations of the different nucleotide states in the penultimate position; but this would require that we explicitly account for the nucleotide distribution in the next position and so on, leading to a combinatorial explosion. We reasoned that for rapidly turning over ends, the fractional (or probability) distribution of nucleotide states in the penultimate position can be approximated by the fraction at the end position, which we do track. As an example, the rate of dissociation of BarbedT to produce BarbedD + GAT would be given by:

$$kr \times \mathrm{BarbedT} \times \frac{\mathrm{BarbedD}}{\mathrm{BarbedT} + \mathrm{BarbedDPi} + \mathrm{BarbedD}} \times S,$$
$$S = 1 - e^{-\frac{\mathrm{FAD}}{\mathrm{Pointed}D}}$$

where kr is the rate constant for dissociation and S is an expression we used to safeguard that the rate is appropriately decreased for filaments too short to contain a sufficient complement of ADP subunits. The analogous expressions were used for dissociation of all the variations on reactants and products for the pointed and barbed ends.

Steady-state simulations before activation of Arp2/3

A Virtual Cell BioModel has a hierarchical structure in which a reaction network, such as that shown in Fig. 1, can spawn several mathematical models (called "applications" within the interface) each with different initial conditions and/or geometry mappings. The mathematics specified in an application can, in turn, spawn many simulations where different time durations or parameter values can be chosen. We created an application called "Steady-State Turnover" in which the variable ActiveNWASP, denoting a generic

nucleation promoting factor, was set to 0 to establish the behavior of the system in the absence of Arp2/3-mediated branching and nucleation. In these circumstances, the spatial distribution of all species will be uniform, so we could formulate the mathematics as a system of ODE. We ran more than 250 simulations with various values of total actin, Cap, profilin, cofilin, ATP/ADP, and thymosin-β4. One objective of these simulations was to validate the model against a number of in vitro studies that were performed at actin concentration of 1 to 20 μM. For example, the simulations are able to precisely recapitulate the average length of actin filaments with or without Cap as well as the effect of including annealing and fragmentation (37,38). They also reproduce the extensive simulations of in vitro experiments reported by Bindschadler et al. (13), where the effect of nucleotide exchange, profilin and thymosin-β4 on actin turnover, filament concentration, and filament length were examined. These validation simulations can be found within the steady-state turnover application in the simulations named: ''turn off fragmentation and annealing, total actin at 10 μM; Cap 0 profilin, bthy, cofilin varied'', ''total actin at 10 μM; Cap 0 Prof, bthy, cofilin varied'', and ''Total Actin at 10 μM; Cap .05; Prof, bthy, cofilin varied''. Because they all scanned several parameters, these tests generated 81 simulations. An additional objective was to establish stable starting concentrations of all the species for simulations of the kinetics after N-WASP-Arp2/3 activated actin polymerization (see below). These simulations were run at physiological concentrations of actin and its modulators—concentrations that are often an order of magnitude higher than those experimentally attainable for in vitro reconstituted systems (54).

Simulations with physiological concentrations of the players, but with inactive Arp2/3, also provided important insights on the interplay of Cap, profilin, and cofilin in modulating actin polymerization. Fig. 2 displays results at 200 μM total actin showing the steady-state values for key variables in the presence of different concentrations of profilin, ADF/cofilin, and Cap. For all these simulations, the actin buffering protein thymosin-β4 was set at 100 μM and allowed to equilibrate with all the G-actin species. As expected, the number and length (Fig. 2, *A* and *B*) of actin filaments is highly sensitive to the presence of Cap, with physiological levels of Cap reducing the average length to several hundred subunits (<1 μm); as might be expected, the severing activity of cofilin also reduces the filament length and increase the concentration of actin filaments, but not as dramatically as Cap. Fig. 2 *C* demonstrates that the turnover rate for assembly of actin at barbed ends and disassembly at pointed ends is highly sensitive to the profilin and cofilin activity: Profilin increases the availability of ATP-G-actin to barbed ends and cofilin increases the concentration of ends. The effect of Cap on filament turnover is more complex, as too little Cap results in a limited supply of free G-actin, but too much Cap limits the supply of free barbed ends. As can be seen in Fig. 2 *D*, the interplay of Cap, profilin, and cofilin is complex, but, generally, Cap increases the available pool of G-actin and cofilin decreases it. Profilin increases the G-actin pool when barbed end concentration is low (no cofilin and high Cap) but can decrease available G-actin when cofilin exposes additional barbed ends. The supply of free G-actin is important, as it provides a limit for how much additional polymerization can occur when Arp2/3 becomes activated in localized regions of the cell. Thus, the baseline behavior in the absence of Arp2/3 activation will help us to understand the behavior of models that include Arp2/3, as described in the following sections.

Effects of Cap and ADF/cofilin on dendritic nucleation

We elaborated the cytosolic actin biochemistry described in the previous section by adding a generic membrane-associated nucleation promoting factor (called ActiveNWASP in our model) to recruit and activate the Arp2/3 complex. We implemented Arp2/3-mediated actin branching and nucleation in two alternative models. The first, (the BioModel entitled ''Actin Dendritic NucleationDetailed Branching'') utilizes (Fig. 1, *left side*) a detailed mechanism recently described by Beltzner and Pollard (23); this mechanism, derived directly from extensive in vitro measurements, explicitly includes an inactive cytoplasmic complex of Arp2/3 with filaments as well as stepwise assembly of the membrane-associated nucleation promoting factor, one G-actin, Arp2/3, and a mother filament, culminating in activation to produce an actively growing branch. In the alternate model, we implemented the reduced mechanism described by Carlsson et al. (21) in which much of the detailed mechanism shown at the left of Fig. 1 is lumped into one step. Specifically, after Arp2/3 is recruited to the membrane and activated by the nucleation promoting factor, one rate expression is used for its binding to F-actin and two G-actin monomers to form a branch with a free barbed end. The reactions at the membrane associated with this lumped mechanism are shown in Fig. S1 in the Supporting Material, and the full model is available as the Virtual Cell BioModel ''Actin Dendritic Nucleation''. We simulated the response of both of these systems to Arp2/3 activation in the presence of varying levels of ActiveNWASP, Arp2/3, Cap, profilin, and cofilin in a series of compartmental (ODE) applications (''NWasp Activation…'') based on a 20 μm diameter spherical cell. All these were for total actin concentrations of 200 μM and thymosin-β4 of 100 μM, using the appropriate steady-state concentrations (derived in the previous section) as initial conditions.

The dynamics of the response to activation is rapid in these simulations ($\leq$30 s); but because these are nonspatial simulations in which the effects of diffusion are not considered, the kinetics of these responses may not be meaningful. Furthermore, local effects such as the accumulation of F-actin in an active lamellipodium, require full spatial

models and are considered in the next section. However, as in the previous section, the magnitude of the response can provide new insights on the interplay of the various modulators of actin assembly. Fig. 3 displays the response of several key variables as a function of different levels of cofilin and Cap. These simulations were generated from the model containing the detailed mechanism for Arp2/3- mediated branching and nucleation (23). The very similar simulation results based on the reduced mechanism (21) are provided in Fig. S2. Comparing these results shows quantitative differences between these two model implementations, but the qualitative trends are the same.

As would be expected, Cap and cofilin have antagonistic effects on the levels of free barbed ends after activation of Arp2/3 (Fig. 3 *A*)—Cap binds to free barbed ends and cofilin exposes new barbed ends by severing. Also consistent with expectation and the general trends in Fig. 2 *D*, increasing Cap and increasing cofilin have opposite effects on the residual G-actin levels after activation of dendritic nucleation (Fig. 3 *B*). But to understand the interplay of cofilin and Cap on the complex pattern for F-actin assembly after dendritic nucleation (Fig. 3 *C*) requires more detailed consideration of these opposing factors, as well as consideration of the initial pool of available G-actin. In the presence of 1 and 2 μM Cap, but 0 cofilin, there is an ample concentration of both free barbed ends (Fig. 3 *A*) and G-actin (Figs. 2 *D* and 3 *B*) to produce a robust increase in F-actin (Fig. 3 *C*); but 4 μM Cap, although actually potentiating the formation of branches (Fig. 3 *D*), blocks barbed ends too completely and quickly after they are formed to permit substantial production of F-actin. In the presence of cofilin, on the other hand, the limiting factor becomes the available G-actin: for 1 μM Cap and 10 μM cofilin, the initial G-actin pool is only 3.5 μM (out of 200 μM), so that despite the ample concentration of barbed ends, relatively little new F-actin production is possible. At 4 μM Cap and 10 μM cofilin, there are sufficient G-actin and barbed end concentrations to allow significant production of new F-actin. The requirement of barbed end capping activity to produce net polymerization upon stimulation of severing activity has been previously argued in a model by Carlsson (18). Indeed, according to Fig. 3 *C*, depending on the Cap concentration, cofilin can either inhibit or enhance the ability of Arp2/3 to increase the level of F-actin. Thus, the model helps to reconcile the frequently conflicting reports on the effect of ADF/cofilin on lamellipodial actin assembly (55-58).

Fig. 3 *D* shows that the concentration of branches (i.e., Arp2/3-associated F-actin) increases with increasing Cap. This is consistent with a recent set of elegant experiments (59) showing that Cap increased Arp2/3 mediated nucleation, but not elongation of filaments. Branch formation (and attendant nucleation) requires active Arp2/3 and 1 actin subunit to combine and bind to a mother filament. At higher Cap concentrations, new barbed ends will be capped before they can soak up the available G-actin, so more of the available monomer is directed toward the assembly of new branches. Clearly, additional biochemical mechanisms and spatial localization will be operative in vivo to further regulate and enhance these effects of Cap and cofilin on dendritic nucleation and can be readily added to the Virtual Cell model. The effects of geometry and spatial localization of ActiveNWASP are illustrated in the next two sections.

A 3D spatial model of actin polymerization at the cell leading edge

To construct a dynamic spatial model of localized polymerization at the leading edge, we used a 3D geometry of a cell with a thin lamellipodium and a thick cell body (Fig. 4) in which the biochemical transformations are combined with diffusion and flow of the molecular species. The resulting system of partial differential equations is governed by mass conservation:

$$\frac{\partial C_i}{\partial t} = -\mathrm{div}_S\,\mathbf{J}_i + R_i, i = 1,\ldots,m$$

$$\mathbf{J}_i = -D_i \mathrm{grad} C_i + \mathrm{v}_i C_i,$$

where C_i is the concentration of the i-th species, $\mathbf{J}_i$ is the diffusive and advective flux density of this species, D_i is the diffusion coefficient, v_i is a velocity vector, and the source term R_i describes the effect of all reactions on the i-th species. Flux at the boundary of the simulation volume was set to 0. The steady-state concentrations, derived under various starting conditions in the Steady State Turnover Application of the *Actin Dendritic Nucleation* BioModel (described above), were used as spatially uniform initial conditions for all the cytosolic species for a Virtual Cell MathModel entitled ''Actin Diffusion and Advection'' to generate the simulations described in this and the following sections. As noted in the previous section, Arp2/3 activation and branching in this model used the reduced mechanism developed by Carlsson (21) because it provided a good approximation to the detailed model (compare Fig. 3 with Fig. S2) and allowed us to use significantly longer time steps in our spatial simulations.

At time 0, an active band of N-WASP in the membrane (Fig. 4) recruits and activates Arp2/3, which in turn binds to F-actin in the cytosol to nucleate growing filament branches (Fig. 1, *left side* (21)). The diffusion coefficient for G-actin, D_{GActin}, was taken as 5 $\mu m^2/s$ based on intracellular measurements (60,61); for simplicity, the same diffusion coefficient was used for all monomeric species including actin-binding proteins. For polymeric actin, a single fixed diffusion coefficient would not be appropriate, given the large spatial and temporal variation in the size and degree of branching of the filaments after localized stimulation of polymerization. Therefore, the F-actin diffusion was modeled according to the following equation:

$$\frac{DG\text{Actin}}{\text{FilamentLength}} * (1 - \text{BranchFraction}).$$

The inverse relationship of diffusion to length for a linear polymer is well established in polymer physical chemistry (38); the FilamentLength at each point in space is calculated from the state variables of the system as the sum of all F-actin species (i.e., the total F-actin) divided by the sum of all pointed end species. To also account for the diminution of diffusion for a highly interconnected branched network, the equation reduces the diffusion coefficient by the fraction of filaments associated with branches; BranchFraction is determined from the state variables as the sum of all the species corresponding to an Arp2/3 capped pointed end bound to a mother F-actin filament, divided by the sum of all the pointed end species (whether Arp2/3 capped or not). This correction effectively produces a weighted average at each mesh point between the F-actin that is detached from the network (with D = $D_{G\text{Actin}}$/FilamentLength) and the F-actin that is part of the dendritic network (with D = 0).

Within the reference frame of a gliding cell (the cell shape is constant), the network of filaments is pushed rearward as actin monomers polymerize near the membrane (6,8).We explicitly modeled the flow of all the F-actin species back from the region of stimulated nucleation, expressed as a velocity field directed radially inward. We reasoned that only those filaments that are connected to the branched network will sense the addition of monomers at the leading edge. Therefore the advective flow within each 335 nm cubic mesh element was made proportional to BranchFraction: $v_i = v_i^{\max} * \text{BranchFraction}$. This treats the flow of all F-actin species in a mesh element as the weighted average of the flow expected for the species that are part of the branched network (with a flow set to the maximal flow at the activated membrane, $v_i^{\max}$) and the species that are part of detached filaments (with a velocity of 0). For the proportionality constant $v_i^{\max}$, i.e., the speed when BranchFraction = 1, we chose a value of 800 nm/min that is close to the average experimentally observed velocity within a band at the cell edge (62,63). Although the velocity should be some function of the rate of filament growth at the leading edge, this growth rate will be constant at the steady state, which is the focus of the simulation results to be presented below.

The resultant 3D model consisted of 48 partial differential equations and 12 algebraic equations, the latter corresponding to fast reactions for which a pseudo-steady-state approximation was applied. Using this combined treatment of diffusion, flow and the biochemical reaction rates within the 3D geometry of Fig. 4, we simulated the localized activation of F-actin nucleation for various concentrations of profilin, cofilin, and Cap. The calculations required 20 days of computer time on a single node in our cluster, but multiple simulations could be run in parallel. A 2D model corresponding to the bottom *xy* plane of the 3D geometry fails to simulate the accumulation of F-actin at the leading edge because it does not provide the reservoir of actin in the rear of the 3D geometry. We also implemented a model in which the entire periphery of the cell was activated instead of the band of activation shown in Fig. 4. This model, described further in the Supporting Material and also available in the Virtual Cell database, has cylindrical symmetry and could therefore be transformed into a mathematically equivalent 2D model that required only 6 h of computer time. It can be used for fast tests of new ideas and for models of cell spreading, where the entire periphery is presumably activated; but, because the nucleation factor was spread rather than concentrated as in Fig. 4, it did not serve as a good model of actin polymerization in a lamellipodium.

Simulation results for key variables in the 3D spatial model

The simulation results in Fig. 5 show standing spatial gradients for the steady-state distribution of total F-actin, velocity (proportional to the distribution of BranchFraction), average filament length, and G-actin·ATP-profilin (GATProf) concentration; these results were for total actin at 200 μM, thymosin-β4 at 100 μM, profilin at 10 μM, Cap at 1 μM, cofilin at 0 μM, and Arp2/3 at 1 μM. Movie S1 showing each variable approaching steady state after activation of the nucleation promoting factor (denoted ''ActiveNWASP'' in our model) is provided in the Supporting Material. The level of ActiveNWASP was graded along the leading edge as shown in Fig. 4. The results for other variables in this simulation as well as 19 additional simulations with varying initial conditions can be found in the Virtual Cell database as described in Methods.

Consistent with experiment (64), local activation of filament assembly through the action of N-WASP and Arp2/3 leads to a large accumulation of F-actin, with a maximum concentration of 725 μM at the tip of the cell. This is accompanied by a net depletion in the rear of the cell to 120 μM, compared to the prestimulus uniform value of 164 μM (Fig. 5, *top row*). It is important to note that we are expressing F-actin as a concentration of subunits, not filaments. To establish how the thickness of the lamellipodium affects the concentration of accumulated F-actin, we also performed simulations in a geometry with a lamellipodium that was a factor of 3 thinner (Fig. S3 in the Supporting Material) than the geometry of Fig. 4; the accumulation of F-actin in this thinner lamellipodium was ~25% greater than in Fig. 5. However, because the thinner lamellipodium has ~1/3 the volume of the lamellipodium in the baseline geometry of Fig. 4, the actual mass of F-actin in the thinner lamellipodium is actually significantly lower.

In additional simulations (available in the Virtual Cell MathModel ''Actin Diffusion and Advection''), we tested how concentrations of Cap at 0.2, 0.5, 1, 2, and 4 μM affect the polymerization of F-actin at the leading edge. Somewhat counterintuitively, the presence of Cap was required for accumulation of F-actin at the leading edge, with even 0.2 μM Cap being insufficient for any significant F-actin buildup. This is

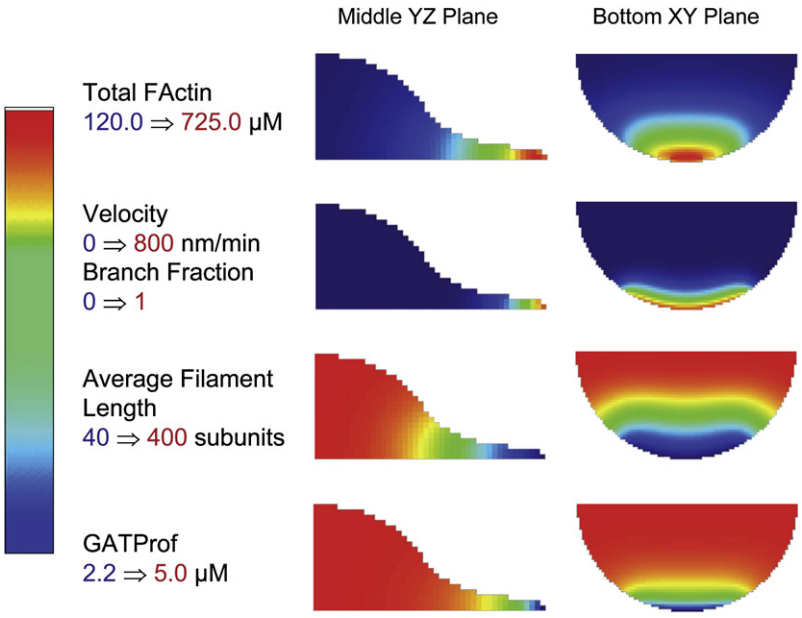

FIGURE 5 Steady-state spatial distributions of key model variables upon activation of dendritic nucleation at the cell edge. The color scale for the minimum (blue) and maximum (red) for each variable is provided under the name of each variable. Total F-actin corresponds to the sum of all species, including ends, that are part of polymerized actin and is given in units of concentration of subunits. The initial uniform Total FActin before activation of dendritic nucleation was 164 μM, so the rear of the cell loses FActin as the front gains. In the model, Velocity is proportional to Branch Fraction, so both show identical distributions but with differing scales; the Branch Fraction is derived from the state variables by dividing the total number of Arp2/3-capped pointed ends (which are part of a branch) by the total concentration of pointed ends. The Average Filament Length is derived by dividing Total FActin by the total concentration of pointed ends; the initial uniform value for this variable before activation is 322 subunits/filament. We also display the distribution of GATProf, that is G-actin associated with ATP and profilin; this is the most active monomeric G-actin species for assembly to barbed ends and is initially at 7.2 μM before activation of dendritic nucleation. Movie S1 shows the approach of all four variables to these steady-state distribution over the first 10 min after activation. The average concentration of the key molecules (sum of all their forms) were: actin, 200 μM; thymosin-β4, 100 μM; profilin, 10 μM; Cap, 1 μM; ADF/cofilin, 0 μM; Arp2/3, 1 μM and ActiveNWASP as specified by the distribution in Fig. 4. The initial concentrations for all the 46 individual species are derived form the corresponding steady state in the absence of ActiveNWASP as determined with a nonspatial (ODE) simulation; these concentrations are provided in Table S3 in the Supporting Material. The geometry was contained in a rectangular domain with x,y,z-dimensions of 30.4 μm, 15.2 μm, and 7.4 μm, respectively; the grid for the numerical simulations contained 90,090 cubic elements with dimensions of 334 nm.

because, as shown in Fig. 2, too low a level of Cap limits the level of prestimulus G-actin that is required for significant additional polymerization after stimulation; this provides an explanation for the observation that lamellipod formation is abolished when Cap is knocked down (65); this simple idea, which emerges from the model, represents an alternative to the ''funneling hypothesis'' (63), but both probably contribute. On the other hand, one might expect that too much Cap would inhibit the assembly at newly formed barbed ends. Indeed the model predicts an optimal accumulation of F-actin at ~1 μM Cap, a level typically found in cells (34) and the concentration chosen for the baseline model of Fig. 5.

The velocity field (Fig. 5, *second row*) has a profile similar to that observed in speckle microscopy measurements (62,63), falling off sharply within 2–3 μm from the leading edge. However, the residual low level of flow that persists for several more micrometers in the experimental data, is absent from the simulations; this has been attributed to actomyosin activity (62), which is not considered in our model. We should also emphasize that our treatment of advection, as described in the previous section, does not explicitly couple the velocity to any force generated by the growing actin filaments in the dendritic network. Therefore, this formulation would not be appropriate for a rigorous study of how the velocity field pattern is affected by modulators of actin polymerization. However, this formulation, in that it produces a velocity profile that is similar to experiment (62,63), does permit us to probe the model for steady-state spatial patterns of the biochemistry. The chosen nominal value of 800 nm/min for the maximum velocity produced F-actin concentrations that increased smoothly up to the activated tip of the cell for a range of concentrations of N-WASP (i.e., stimulus strength), profilin, cofilin, and Cap. Choosing a larger value for this parameter caused the steady-state F-actin concentration to spread and to peak away from the leading edge; a lower value caused a more concentrated and condensed band of F-actin at the front of the stimulated lamellipodium (data not shown but available in the Virtual Cell MathModel, ''Actin Advection and Diffusion'').

The rapid assembly of F-actin in the restricted diffusive space of the lamellipodium causes a local depletion of ATP-G-actin bound to profilin (GATProf, Fig. 5, *fourth row*), the most reactive of the G-actin monomer species. The delivery of G-actin can significantly limit the rate of dendritic nucleation at the activated tip of the cell, and evidence has been presented that active motor-driven transport of G-actin may occur (60). However both our model and the results of a more targeted modeling study of this issue (17) indicate that diffusion of G-actin is sufficient for delivery of new monomer to the actively polymerizing actin at the leading edge. The absence of a G-actin gradient during the initial stages of activation produce an overshoot in F-actin concentration at the lamellipodium that then settles to the steady-state level (see Movie S1).

The small average length of filaments near the activated edge (Fig. 5, *third row*) is consistent with electron microscope images of lamellipodia (9). The average length at the tip of the cell is 40 subunits/filament and 400 subunits/filament in the

rear at steady state. This pattern is produced by rapid nucleation and capping of new filaments in this region. New barbed ends can either elongate through the addition of G-actin or be capped; this competition is biased toward capping in the activated lamellipodium because of the local depletion of G-actin, as discussed above. The concentration of filaments (not shown, but given by dividing total F-actin by the average length) is even more biased toward the leading edge, with ~16 μM filaments in the front and 0.3 μM in the rear. Interestingly, the overall depletion of free Cap in the cell actually causes an increase in the average filament length to 400 subunits/filament in the rear, from an initial prestimulus level of 320 subunits/filament (see Movie S1).

The sharp lamellipodial assembly-disassembly transition emerges from actin biochemistry

We examined the rate of polymerization and depolymerization in Fig. 6. Fig. 6 *a* shows the steady-state distribution of the rate of addition of actin subunits to filaments (negative values indicate loss of actin from filaments), in units of μM/s, at a plane corresponding to the bottom *xy* plane of the 3D geometry. As expected, the rate of assembly is sharply peaked at the activated edge of the cell. Fig. 6 *b* shows the same simulation results with a color scale that displays all positive rates in white and all negative rates, i.e., net disassembly, in color, with the most negative values in blue and a rate of 0 μM/s in red. This pattern is not significantly changed for a geometry in which the lamellipodium is thinned by a factor of 3 (see Fig. S3). Thus, the model reproduces the sharp boundary between actin filament assembly and disassembly that was discovered with the speckle microscopy experiments (62,63,65,66) and that occurs ~1 μm from the activated edge. (See, for example, Fig. 3 a. in Ponti et al. (63)). The steady-state distribution of free pointed ends, Fig. 6 *c*, provides an explanation for this behavior. Whereas the free barbed end distribution is strongly peaked at the activated edge, decreasing rapidly and monotonically toward the interior, the free pointed end distribution rises to a peak at 2 μm from the cell edge and only then declines toward the interior. Because free barbed ends are prone to assembly and pointed ends to disassembly, the rapid transition at ~1 μm from the leading edge follows. We used the measured rate constants of Arp2/3 debranching (24) in our model, and the position of the assembly-disassembly transition is particularly sensitive to these parameters. This is because debranching is

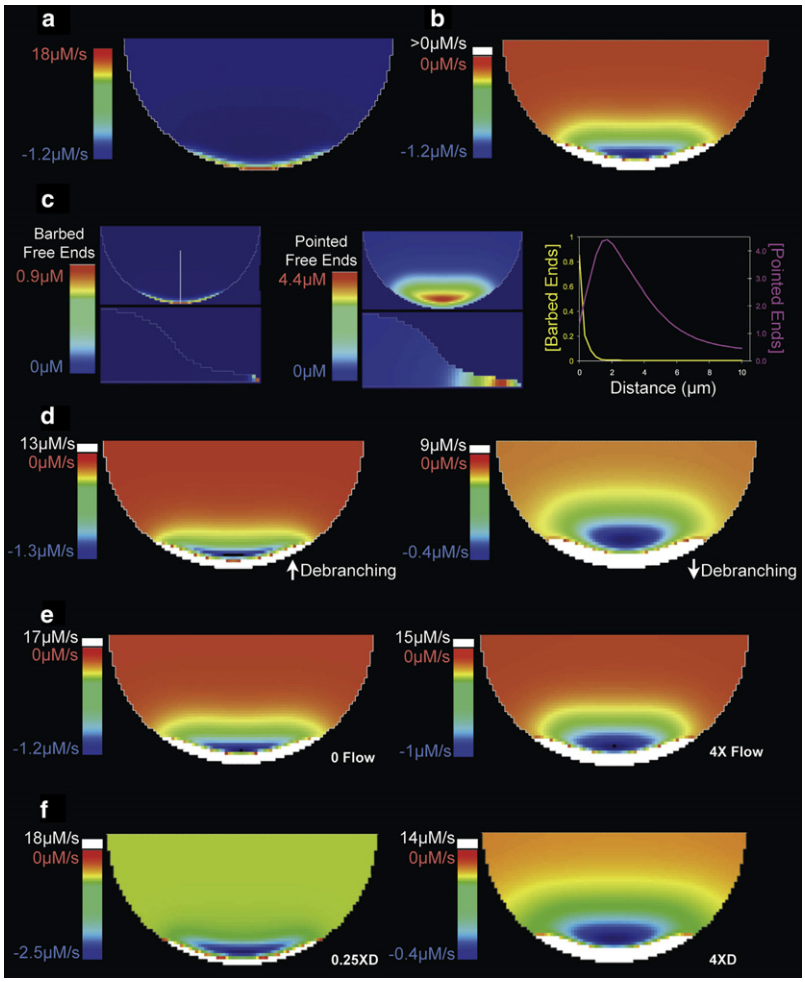

FIGURE 6 The rate of filament growth displays a sharp boundary between polymerization and depolymerization 1 μm from the cell edge. (*a*) A slice from the bottom *xy* plane of the 3D geometry shows the steady-state rate of assembly sharply peaking at the activated edge of the cell. (*b*) The same values as in *a* are mapped to a new color scale in which all the positive values are white and negative values are mapped from blue (−1.2 μM/s) to red (balanced assembly and disassembly). (*c*) The steady-state distribution of free barbed ends and free pointed ends mirror the regions of highest actin assembly and disassembly, respectively (*top*, lowest *XY* plane; *bottom*, central *YZ* plane. The plot to the right shows the concentration of ends as a function of distance along a line emanating from the edge toward the middle of the cell (superposed on the image in the *upper left panel*). (*d*) Steady-state distribution of assembly rates when the rate constants for dissociation of branches from ATP-bound and ADPPi-bound subunits on mother filaments are increased by a factor of 5 to match the normally faster rate constant for dissociation from ADP-bound subunits (24) (*left*) or when all the debranching rate constants are decreased by a factor of 4 (*right*). (*e*) Steady-state distribution of assembly rates when F-actin flow is turned off (*left*) or when the velocity field is set equal to 3200 nm/min **BranchFraction* (*right*); the latter is four times the nominal flow rate that was used for all the other simulations. (*f*) Steady-state distribution of assembly rates when the proportionality constant, D_{GActin} in the equation for F-actin diffusion coefficient is changed from the nominal value of 5 $\mu m^2/s$ as indicated; note that the actual diffusion coefficient of monomeric species remained at 5 $\mu m^2/s$ in these simulations. The initial concentrations and simulation details were identical to those of Fig. 5.

accompanied by dissociation of the Arp2/3 cap from the pointed ends, thus exposing high concentrations of these rapidly disassembling ends. In the kinetic measurements, debranching is most rapid from a mother filament if the Arp2/3 is attached to F-actin in the ADP-bound form, with the ATP and ADPPi forms displaying a fivefold slower rate (24). The sensitivity to these parameters is demonstrated by equalizing the rates of all three forms to the rapid ADP rate (Fig. 6 *d*, *left*); this moves the transition ~50% closer to the stimulated edge where the younger ATP- and ADPPi-F-actin is prevalent. Conversely, a numerical experiment in which all these rates are decreased by a factor of 4 (Fig. 6 *d*, *right*) moves the transition point much further into the cell interior and also spreads a diminished disassembly rate over a broader area of the cell.

The interplay of debranching rate and the rearward displacement (via a combination of diffusion and advection) of newly formed F-actin should account for the filament turnover pattern, but this requires additional analysis. With regard to advection, it is interesting to analyze how sensitive the pattern of filament turnover is to the maximum advection rate at a newly formed branch, 800 nm/min for the nominal model. This value is related to the rate of addition of monomer to an average barbed end at the leading edge of the cell: the rate of polymerization at the leading edge (18 μM/s, Fig. 6 *a*) divided by the concentration of barbed ends (0.85 μM, Fig. 6 *c*, *left*), or 0.21 s^{-1}; if all of this were converted to a flow of the branched network, the velocity at that spatial location would be given by multiplying by the length of an actin subunit, 0.0026 μm. The resultant velocity of 3.3 μm/min represents an upper bound as it does not account for the distribution of filament orientation angles with respect to the edge normal and it does not account for the compressibility of the actin gel or the elasticity of the membrane. Thus, we feel that the chosen value of 0.8 μm/min is reasonably self-consistent with the calculated maximal steady-state filament turnover rate. Further away from the edge, one might anticipate a negative feedback effect on the advection rate because of its dependence, in our model, on the branch fraction at a mesh point. That is, as debranching occurs, filaments that are released from the assembling dendritic network become disconnected from the source of rearward flow; this is modeled in our formulation as a proportional decrease in the average flow rate of all F-actin species, which provides more time for debranching before the flow sweeps the actin further back. Indeed, the distribution of F-actin is highly sensitive to the advection rate (data not shown, but available in the public Virtual Cell model). Surprisingly, therefore, the position of the boundary between assembly and disassembly is not at all sensitive to the choice of maximum advection velocity. As shown in the results of the numerical experiments displayed in Fig. 6 *e*, the position of the boundary between assembly and disassembly does not move from the nominal position at 1 μm from the edge (Fig. 6 *b*) even when flow is completely eliminated, but moves slightly toward the cell interior only when the flow rate is increased by a factor of 4 (to a maximum of 3200 nm/min, close to the upper bound value for advection calculate for the nominal model). This insensitivity is also important because the choice of nominal maximum advection rate (800 nm/min) was based on the experimentally observed velocity field (63) in a cell whose composition of actin and actin-binding proteins may differ from the nominal values assumed in this model. Indeed, additional simulations were performed with variations in actin, thymosin-β4, Cap, cofilin, and profilin concentrations (available in the public Virtual Cell model) with very little effect on the pattern of filament turnover, although there were significant changes in F-actin accumulations. This insensitivity can be understood because of a counterbalancing positive-feedback effect of F-actin concentration on the branching rate at the activated region of membrane: as more F-actin is produced by branch-dependent nucleation, more branches are formed because they require association of activated Arp2/3 with F-actin. Therefore, changes to the maximal advection rate produces compensatory changes in the rate of debranching (linked to disassembly) and the rate of branching (linked to assembly). By contrast, Fig. 6 *f* demonstrates that the pattern of F-actin assembly and disassembly is quite sensitive to the diffusion coefficient chosen to represent a filament with just one subunit, i.e., D_{GActin}. Reducing this proportionality constant by a factor of 4 brings the boundary between assembly and disassembly to ~0.5 μm from the leading edge and increasing it by a factor of 4 moves the boundary to ~2 μm from the leading edge. As expected the value of D_{FActin} is quite low throughout the simulation volume, maximizing at a value of only 0.035 $\mu m^2/s$ at 2 μm away from the leading edge for the nominal simulation parameters. But these results show that F-actin diffusion is required to move the debranching region away from the cell edge in this range of advection speeds.

DISCUSSION

This work establishes that quantitative biochemical data on the components of the actin dendritic nucleation system, derived painstakingly from numerous in vitro experiments on all the individual steps, can help unravel the complexity of the spatial/temporal patterns observed in the lamellipodia of living cells.

1. The model reproduces the steady-state accumulation of high densities of F-actin at the leading edge (64).
2. The model is able to suggest a way to reconcile conflicting experimental results on the role of ADF/cofilin as either a promoter (55,58) or inhibitor (56,57) of Arp2/3-mediated actin polymerization. The model predicts that if the level of Cap is knocked down, cofilin should inhibit actin polymerization; when Cap is overexpressed, cofilin should enhance actin polymerization. Likewise, Cap can either promote or retard actin polymerization depending on how it is coordinated with cofilin activity.

3. Without invoking any specialized zones within the lamellipodium, the model generates the sharp boundary between polymerization and depolymerization discovered by speckle microscopy experiments (62,63,65,66). The model helps to explain how this behavior can be understood as emerging from an interplay of rearward flow of the actin network, barbed end capping, and dissociation of Arp2/3 branches to expose free pointed ends. In particular, the model predicts that stabilizing Arp2/3 branches should move the boundary toward the rear and decrease its sharpness.

The sensitivity of the system to the rate of Arp2/3 branch dissociation illustrates how modeling and simulation can be used to determine which rates and concentrations are the most important regulators of the biology and how the biology can be very robust to variations in other parameters. This is especially remarkable given the omission from the model of other potentially important players, such as the formins, tropomyosin, and myosin. Indeed, recent studies indicate that these species are largely inactive in the lamellipodium and may be confined to the lamellum (65,67–69). Important physics that is not explicitly treated by our model include mechanical forces and the nonideal crowded environment of the cell. In particular, we made no attempt to directly relate the advective flow of F-actin to mechanical forces or the viscoelastic properties of the cytoplasm; we incorporated, instead, a phenomenological specification for the flow as being proportional to the fraction of F-actin in branches, reasoning that only those filaments connected to the branched network could be pushed back by growing filaments at the tip. It should also be emphasized that although we made every attempt to derive biochemical rates and parameters from the literature (Table S2), these values can vary greatly from cell type to cell type and even from laboratory to laboratory.

Perhaps most importantly, mechanisms that are derived from in vitro or in vivo experiments may be missing some key players that can completely alter the system behavior. This point is perhaps best exemplified by the growing literature on the complex mechanism of the action of ADF/cofilin in controlling F-actin assembly at the leading edge. In our model, we used mechanisms and rate parameters derived from careful in vitro studies of active (i.e., unphosphorylated) cofilin (42,45). From our nonspatial model (Fig. 3), we were able to conclude that cofilin could either promote or inhibit Arp2/3-mediated F-actin accumulation, depending on the level of barbed end capping activity; this is consistent with a previous modeling study that showed that stimulation of polymerization by severing required capping (18). But a more recent in vitro study produces a much more complex picture in which cofilin severs at low concentrations but acts as a nucleator at high concentrations (47). Furthermore, combined experiments on Listeria monocytogenes actin comet tails identified two additional mediators, Aip1 and coronin, which were required to assist cofilin in disassembling F-actin (70). Indeed, our simulations, which do not include these additional activities because their rate laws have not yet been determined, produce a decrease in the level of G-actin in the presence of cofilin (Figs. 2 and 3). The contribution of these factors to the in vivo behavior are further complicated by the spatial moduation of cofilin activity by other actin-binding proteins such as tropomyosin (71) or by localized signaling (72,73). All this complexity certainly challenges our ability to develop quantitative predictive models, but also motivates modeling as the best means to help organize the data and guide its interpretation.

Thus, any mechanistic biophysical model of a complex cellular process is necessarily approximate and includes assumptions and compromises to assure that the model is not so complex that it becomes analytically intractable or computationally prohibitive. We felt it was important to model a full 3D geometry incorporating the thin lamellipodium, where the dendritic nucleation process is active, and the large volume of the rest of the cell, which serves as a dynamic reservoir of G-actin. Although there have been several important insights that have been developed through discrete simulations, which consider the G-actin pool as continuously distributed and cover just a small intracellular volume (10,74,75), the large number of molecules in a whole cell model (200 μM actin within our 3D volume translates to 10^8 molecules) precludes a discrete stochastic approach because such simulations would be computationally prohibitive. Additionally, much of the detail from a stochastic simulation is not required to interpret the experimental patterns of fluorescence. However, a continuous model of actin polymerization, where there is a distribution of polymer lengths, nucleotide distributions within filaments, and levels of branching, requires decisions about which species or states of actin to treat explicitly and which to lump. We decided to incorporate as much of the known detailed biochemistry as possible, e.g., explicitly treating the three nucleotide-bound forms of every actin species.

The most computationally intensive simulations that we performed were on the 3D instantiation of our model, where 4000 s was simulated to assure that the steady-state distributions of all the model components had been attained (Figs. 5 and 6). These simulations required 20 days on a single Intel Xeon processor. But many such simulations with differing levels of the key actin-binding proteins could be run simultaneously on our computer cluster. Simulations of dynamics starting from the steady state will require a much shorter duration. Furthermore, many ideas can be tested with ODE simulations, such as those that produced Figs. 2 and 3, which each took only seconds to run. Thus, new ideas can be readily and fully explored before they are tested in the laboratory.

Indeed, to the extent that modeling and simulation can help guide the design of key experiments, they should be of great value for laboratory cell biologists. Clamping

a molecular species to a fixed or time varying value, disabling individual reactions, or systematically simulating the model with a range of initial concentrations of several molecules can all be achieved with a few mouse clicks with the Virtual Cell user interface. Likewise, variations of the model with changes in the reaction network can be readily implemented, and linking different geometries to the reaction network can be achieved in seconds. Thus, the model can provide insight into the key steps that control the system behavior by permitting ''virtual experiments'' such as the manipulation of rate constants or performing virtual knockdowns of key molecules. The model makes predictions (such as the steady-state spatial distribution of barbed and pointed ends or the requirement for Cap to assure the availability of a pool of G-actin) that can be tested experimentally. Additionally, the ability of the model to gather and organize all the experimental information is itself a significant product of this effort. The model can be reused to explore the roles of other key players in actin polymerization. Indeed, because model components such as individual reactions, geometries, and simulations are available through the Virtual Cell public database, this work can serve as a jumping off point for the construction of new models that could incorporate other aspects of actin cell biology or couple the activation of actin polymerization to signaling pathways.

SUPPORTING MATERIAL

Three tables, three figures, a narrative description of model components, and one movie are available at http://www.biophysj.org/biophysj/supplemental/S0006-3495(09)00550-5.

This study benefited greatly from discussions with Thomas Pollard, Boris Slepchenko, Pavel Kraikivski, Mark Zajac, and Charles Wolgemuth.

This work was supported by U.S. Public Health Service grants from the National Center for Research Resources (P41 RR013186), the National Institutes of Health Roadmap National Technology Centers for Networks and Pathways (U54 RR022232), and the National Institute for General Medical Sciences through the Cell Migration Consortium (U54 GM64346).

REFERENCES

1. Millard, T. H., S. J. Sharp, and L. M. Machesky. 2004. Signalling to actin assembly via the WASP (Wiskott-Aldrich syndrome protein)-family proteins and the Arp2/3 complex. *Biochem. J.* 380:1–17.
2. Goley, E. D., and M. D. Welch. 2006. The ARP2/3 complex: an actin nucleator comes of age. *Nat. Rev. Mol. Cell Biol.* 7:713–726.
3. Pollard, T. D. 2007. Regulation of actin filament assembly by arp2/3 complex and formins. *Annu. Rev. Biophys. Biomol. Struct.* 36:451–477.
4. Pollard, T. D., and G. G. Borisy. 2003. Cellular motility driven by assembly and disassembly of actin filaments. *Cell.* 112:453–465.
5. Carlier, M. F., and D. Pantaloni. 2007. Control of actin assembly dynamics in cell motility. *J. Biol. Chem.* 282:23005–23009.
6. Mogilner, A., and G. Oster. 2003. Force generation by actin polymerization II: the elastic ratchet and tethered filaments. *Biophys. J.* 84:1591–1605.
7. Mogilner, A. 2006. On the edge: modeling protrusion. *Curr. Opin. Cell Biol.* 18:32–39.
8. Mogilner, A., and G. Oster. 1996. Cell motility driven by actin polymerization. *Biophys. J.* 71:3030–3045.
9. Svitkina, T. M., and G. G. Borisy. 1999. Arp2/3 complex and actin depolymerizing factor/cofilin in dendritic organization and treadmilling of actin filament array in lamellipodia. *J. Cell Biol.* 145:1009–1026.
10. Schaus, T. E., E. W. Taylor, and G. G. Borisy. 2007. Self-organization of actin filament orientation in the dendritic-nucleation/array-treadmilling model. *Proc. Natl. Acad. Sci. USA.* 104:7086–7091.
11. Schaus, T. E., and G. G. Borisy. 2008. Performance of a population of independent filaments in lamellipodial protrusion. *Biophys. J.* 95:1393–1411.
12. Michelot, A., J. Berro, C. Guerin, R. Boujemaa-Paterski, C. J. Staiger, et al. 2007. Actin-filament stochastic dynamics mediated by ADF/cofilin. *Curr. Biol.* 17:825–833.
13. Bindschadler, M., E. A. Osborn, C. F. Dewey, Jr., and J. L. McGrath. 2004. A mechanistic model of the actin cycle. *Biophys. J.* 86:2720–2739.
14. Mogilner, A., and L. Edelstein-Keshet. 2002. Regulation of actin dynamics in rapidly moving cells: a quantitative analysis. *Biophys. J.* 83:1237–1258.
15. Dawes, A. T., and L. Edelstein-Keshet. 2007. Phosphoinositides and rho proteins spatially regulate actin polymerization to initiate and maintain directed movement in a one-dimensional model of a motile cell. *Biophys. J.* 92:744–768.
16. Keren, K., Z. Pincus, G. M. Allen, E. L. Barnhart, G. Marriott, et al. 2008. Mechanism of shape determination in motile cells. *Nature.* 453:475–480.
17. Novak, I. L., B. M. Slepchenko, and A. Mogilner. 2008. Quantitative analysis of G-actin transport in motile cells. *Biophys. J.* 95:1627–1638.
18. Carlsson, A. E. 2006. Stimulation of actin polymerization by filament severing. *Biophys. J.* 90:413–422.
19. Pollard, T. D. 2002. The future of biomedical research: from the inventory of genes to understanding physiology and the molecular basis of disease. *JAMA.* 287:1725–1727.
20. Marchand, J. B., D. A. Kaiser, T. D. Pollard, and H. N. Higgs. 2001. Interaction of WASP/Scar proteins with actin and vertebrate Arp2/3 complex. *Nat. Cell Biol.* 3:76–82.
21. Carlsson, A. E., M. A. Wear, and J. A. Cooper. 2004. End versus side branching by Arp2/3 complex. *Biophys. J.* 86:1074–1081.
22. Chhabra, E. S., and H. N. Higgs. 2007. The many faces of actin: matching assembly factors with cellular structures. *Nat. Cell Biol.* 9:1110–1121.
23. Beltzner, C. C., and T. D. Pollard. 2008. Pathway of actin filament branch formation by Arp2/3 complex. *J. Biol. Chem.* 283:7135–7144.
24. Mahaffy, R. E., and T. D. Pollard. 2006. Kinetics of the formation and dissociation of actin filament branches mediated by Arp2/3 complex. *Biophys. J.* 91:3519–3528.
25. Kinosian, H. J., L. A. Selden, L. C. Gershman, and J. E. Estes. 2000. Interdependence of profilin, cation, and nucleotide binding to vertebrate non-muscle actin. *Biochemistry.* 39:13176–13188.
26. Blanchoin, L., and T. D. Pollard. 2002. Hydrolysis of ATP by polymerized actin depends on the bound divalent cation but not profilin. *Biochemistry.* 41:597–602.
27. Melki, R., S. Fievez, and M. F. Carlier. 1996. Continuous monitoring of Pi release following nucleotide hydrolysis in actin or tubulin assembly using 2-amino-6-mercapto-7-methylpurine ribonucleoside and purine-nucleoside phosphorylase as an enzyme-linked assay. *Biochemistry.* 35:12038–12045.
28. Fujiwara, I., D. Vavylonis, and T. D. Pollard. 2007. Polymerization kinetics of ADP- and ADP-Pi-actin determined by fluorescence microscopy. *Proc. Natl. Acad. Sci. USA.* 104:8827–8832.
29. Pollard, T. D., and J. A. Cooper. 1986. Actin and actin-binding proteins. A critical evaluation of mechanisms and functions. *Annu. Rev. Biochem.* 55:987–1035.

30. Kinosian, H. J., L. A. Selden, L. C. Gershman, and J. E. Estes. 2002. Actin filament barbed end elongation with nonmuscle MgATP-actin and MgADP-actin in the presence of profilin. *Biochemistry.* 41:6734–6743.

31. Godschmidt-Clermont, P. J., L. M. Machesky, S. K. Doberstein, and T. D. Pollard. 1991. Mechanism of the interaction of human platelet profilin with actin. *J. Cell Biol.* 113:1081–1089.

32. Blanchoin, L., and T. D. Pollard. 1998. Interaction of actin monomers with Acanthamoeba actophorin (ADF/cofilin) and profilin. *J. Biol. Chem.* 273:25106–25111.

33. Kang, F., D. L. Purich, and F. S. Southwick. 1999. Profilin promotes barbed-end actin filament assembly without lowering the critical concentration. *J. Biol. Chem.* 274:36963–36972.

34. Wear, M. A., and J. A. Cooper. 2004. Capping protein: new insights into mechanism and regulation. *Trends Biochem. Sci.* 29:418–428.

35. Schafer, D., P. Jennings, and J. Cooper. 1996. Dynamics of capping protein and actin assembly in vitro: uncapping barbed ends by polyphosphoinositides. *J. Cell Biol.* 135:169–179.

36. Kuhn, J. R., and T. D. Pollard. 2007. Single molecule kinetic analysis of actin filament capping: polyphosphoinositides do not dissociate capping proteins. *J. Biol. Chem.* 282:28014–28024.

37. Andrianantoandro, E., L. Blanchoin, D. Sept, J. A. McCammon, and T. D. Pollard. 2001. Kinetic mechanism of end-to-end annealing of actin filaments. *J. Mol. Biol.* 312:721–730.

38. Sept, D., J. Xu, T. D. Pollard, and J. A. McCammon. 1999. Annealing accounts for the length of actin filaments formed by spontaneous polymerization. *Biophys. J.* 77:2911–2919.

39. Carlier, M. F., C. Jean, K. J. Rieger, M. Lenfant, and D. Pantaloni. 1993. Modulation of the interaction between G-actin and thymosin beta 4 by the ATP/ADP ratio: possible implication in the regulation of actin dynamics. *Proc. Natl. Acad. Sci. USA.* 90:5034–5038.

40. Nachmias, V. T. 1993. Small actin-binding proteins: the beta-thymosin family. *Curr. Opin. Cell Biol.* 5:56–62.

41. Ressad, F., D. Didry, G. X. Xia, Y. Hong, N. H. Chua, et al. 1998. Kinetic analysis of the interaction of actin-depolymerizing factor (ADF)/cofilin with G- and F-actins. Comparison of plant and human ADFs and effect of phosphorylation. *J. Biol. Chem.* 273:20894–20902.

42. Blanchoin, L., and T. D. Pollard. 1999. Mechanism of interaction of Acanthamoeba actophorin (ADF/Cofilin) with actin filaments. *J. Biol. Chem.* 274:15538–15546.

43. Ressad, F., D. Didry, C. Egile, D. Pantaloni, and M. F. Carlier. 1999. Control of actin filament length and turnover by actin depolymerizing factor (ADF/cofilin) in the presence of capping proteins and ARP2/3 complex. *J. Biol. Chem.* 274:20970–20976.

44. Blanchoin, L., T. D. Pollard, and R. D. Mullins. 2000. Interactions of ADF/cofilin, Arp2/3 complex, capping protein and profilin in remodeling of branched actin filament networks. *Curr. Biol.* 10:1273–1282.

45. Cao, W., J. P. Goodarzi, and E. M. De La Cruz. 2006. Energetics and kinetics of cooperative cofilin-actin filament interactions. *J. Mol. Biol.* 361:257–267.

46. Cai, L., T. W. Marshall, A. C. Uetrecht, D. A. Schafer, and J. E. Bear. 2007. Coronin 1B coordinates Arp2/3 complex and cofilin activities at the leading edge. *Cell.* 128:915–929.

47. Andrianantoandro, E., and T. D. Pollard. 2006. Mechanism of actin filament turnover by severing and nucleation at different concentrations of ADF/cofilin. *Mol. Cell.* 24:13–23.

48. Moraru, I. I., J. C. Schaff, B. M. Slepchenko, M. Blinov, F. Morgan, et al. 2008. The virtual cell modeling and simulation software environment. *IET Systems Biology.* 2:352–362.

49. Schaff, J., C. C. Fink, B. Slepchenko, J. H. Carson, and L. M. Loew. 1997. A general computational framework for modeling cellular structure and function. *Biophys. J.* 73:1135–1146.

50. Slepchenko, B. M., J. C. Schaff, I. G. Macara, and L. M. Loew. 2003. Quantitative cell biology with the. *Virtual Cell. Trends Cell Biol.* 13:570–576.

51. Novak, I. L., F. Gao, Y. S. Choi, D. Resasco, J. C. Schaff, et al. 2007. Diffusion on a curved surface coupled to diffusion in the volume: application to cell biology. *J. Comput. Phys.* 226:1271–1290.

52. Schaff, J. C., B. M. Slepchenko, Y. Choi, J. M. Wagner, D. Resasco, et al. 2001. Analysis of non-linear dynamics on arbitrary geometries with the Virtual Cell. *Chaos.* 11:115–131.

53. Slepchenko, B. M., J. C. Schaff, and Y. S. Choi. 2000. Numerical approach to fast reaction-diffusion systems: application to buffered calcium waves in bistable models. *J. Comput. Phys.* 162:186–218.

54. dos Remedios, C. G., D. Chhabra, M. Kekic, I. V. Dedova, M. Tsubakihara, et al. 2003. Actin binding proteins: regulation of cytoskeletal microfilaments. *Physiol. Rev.* 83:433–473.

55. DesMarais, V., M. Ghosh, R. Eddy, and J. Condeelis. 2005. Cofilin takes the lead. *J. Cell Sci.* 118:19–26.

56. Nishita, M., C. Tomizawa, M. Yamamoto, Y. Horita, K. Ohashi, et al. 2005. Spatial and temporal regulation of cofilin activity by LIM kinase and Slingshot is critical for directional cell migration. *J. Cell Biol.* 171:349–359.

57. Hotulainen, P., E. Paunola, M. K. Vartiainen, and P. Lappalainen. 2005. Actin-depolymerizing factor and cofilin-1 play overlapping roles in promoting rapid F-actin depolymerization in mammalian nonmuscle cells. *Mol. Biol. Cell.* 16:649–664.

58. Kiuchi, T., K. Ohashi, S. Kurita, and K. Mizuno. 2007. Cofilin promotes stimulus-induced lamellipodium formation by generating an abundant supply of actin monomers. *J. Cell Biol.* 177:465–476.

59. Akin, O., and R. D. Mullins. 2008. Capping protein increases the rate of actin-based motility by promoting filament nucleation by the Arp2/3 complex. *Cell.* 133:841–851.

60. Zicha, D., I. M. Dobbie, M. R. Holt, J. Monypenny, D. Y. H. Soong, et al. 2003. Rapid actin transport during cell protrusion. *Science.* 300:142–145.

61. McGrath, J. L., Y. Tardy, C. F. Dewey, Jr., J. J. Meister, and J. H. Hartwig. 1998. Simultaneous measurements of actin filament turnover, filament fraction, and monomer diffusion in endothelial cells. *Biophys. J.* 75:2070–2078.

62. Ponti, A., M. Machacek, S. L. Gupton, C. M. Waterman-Storer, and G. Danuser. 2004. Two distinct actin networks drive the protrusion of migrating cells. *Science.* 305:1782–1786.

63. Ponti, A., A. Matov, M. Adams, S. Gupton, C. M. Waterman-Storer, et al. 2005. Periodic patterns of actin turnover in lamellipodia and lamellae of migrating epithelial cells analyzed by quantitative fluorescent speckle microscopy. *Biophys. J.* 89:3456–3469.

64. Abraham, V. C., V. Krishnamurthi, D. L. Taylor, and F. Lanni. 1999. The actin-based nanomachine at the leading edge of migrating cells. *Biophys. J.* 77:1721–1732.

65. Iwasa, J. H., and R. D. Mullins. 2007. Spatial and temporal relationships between actin-filament nucleation, capping, and disassembly. *Curr. Biol.* 17:395–406.

66. Carlier, M. F., and D. Pantaloni. 1997. Control of actin dynamics in cell motility. *J. Mol. Biol.* 269:459–467.

67. Schaub, S., S. Bohnet, V. M. Laurent, J.-J. Meister, and A. B. Verkhovsky. 2007. Comparative maps of motion and assembly of filamentous actin and myosin ii in migrating cells. *Mol. Biol. Cell.* 18:3723–3732.

68. Yam, P. T., C. A. Wilson, L. Ji, B. Hebert, E. L. Barnhart, et al. 2007. Actin myosin network reorganization breaks symmetry at the cell rear to spontaneously initiate polarized cell motility. *J. Cell Biol.* 178:1207–1221.

69. Gupton, S. L., K. Eisenmann, A. S. Alberts, and C. M. Waterman-Storer. 2007. mDia2 regulates actin and focal adhesion dynamics and organization in the lamella for efficient epithelial cell migration. *J. Cell Sci.* 120:3475–3487.

70. Brieher, W. M., H. Y. Kueh, B. A. Ballif, and T. J. Mitchison. 2006. Rapid actin monomer-insensitive depolymerization of Listeria actin comet tails by cofilin, coronin, and Aip1. *J. Cell Biol.* 175: 315–324.

71. Gupton, S. L., K. L. Anderson, T. P. Kole, R. S. Fischer, A. Ponti, et al. 2005. Cell migration without a lamellipodium: translation of actin dynamics into cell movement mediated by tropomyosin. *J. Cell Biol.* 168:619–631.

72. Delorme, V., M. Machacek, C. DerMardirossian, K. L. Anderson, T. Wittmann, et al. 2007. Cofilin activity downstream of Pak1 regulates cell protrusion efficiency by organizing lamellipodium and lamella actin networks. *Dev. Cell.* 13:646–662.

73. Frantz, C., G. Barreiro, L. Dominguez, X. Chen, R. Eddy, et al. 2008. Cofilin is a pH sensor for actin free barbed end formation: role of phosphoinositide binding. *J. Cell Biol.* 183:865–879.

74. Alberts, J. B., and G. M. Odell. 2004. In silico reconstitution of Listeria propulsion exhibits nano-saltation. *PLoS Biol.* 2:e412.

75. Schaus, T. E., and G. G. Borisy. 2008. Performance of a population of independent filaments in lamellipodial protrusion. *Biophys. J.* 95:1393–1411.